The Calculation of Negative Bias Illumination Stress-Induced Instability of Amorphous InGaZnO Thin-Film Transistors for Instability-Aware Design

Jun Tae Jang, Sung-Jin Choi, Dong Myong Kim, *Member, IEEE,* and Dae Hwan Kim, *Senior Member, IEEE*

***Abstract*— We propose a systematic calculation method for negative bias illumination stress (NBIS)-induced instabilities in amorphous InGaZnO thin-film transistors (TFTs). The proposed method is based on activation energy window (AEW) in subgap energy range, and it can reproduce the NBIS time evolution of *I–V* characteristics without long-term stress test. Furthermore, it quantitatively explains the effect of oxygen content on the NBIS instability. The AEW, which is employed for emulating the oxygen vacancy ionization, peroxide formation, and hole trapping, has the order of magnitude of 10^{16}–10^{17} cm^{-3} for the bias stress of −20 V and the commercial LED backlight of 300 cd/m^2. The proposed method is expected to play such an important role in the instability awareness of amorphous oxide TFTs.**

***Index Terms*— Activation energy window (AEW), InGaZnO, instability, negative bias illumination stress (NBIS), thin-film transistors (TFTs).**

I. Introduction

AMORPHOUS indium-gallium-zinc-oxide (a-IGZO) thin-film transistors (TFTs) have attracted much attention due to its advantages, such as high field-effect mobility (μ_{FE}), low subthreshold swing (SS), high ON current, and low OFF current, as promising candidates for switching or driving devices in the field of flat panel displays [1]–[3]. However, various instabilities under bias/illumination stress remain as challenging issues in terms of commercialization [2], [3]. To date, many researchers have qualitatively studied on mechanisms of the negative bias illumination stress (NBIS) instability in a-IGZO TFTs, which have been attributed to the positively charged trapping model only with the negative shift of threshold voltage (V_T) [4], [5], and to the oxygen vacancy (V_O) ionization model leading to both the negative shift of the V_T and degradation of the μ_{FE} as well as the SS [6], [7]. Recently, Nahm *et al.* [8] have proposed a metastable peroxide formation model leading to the negative shift of the V_T to explain the NBIS-based instability in relation to persistent photoconductivity [8]. However, the quantitative analysis on the NBIS-induced V_T shift (ΔV_T) has not been thoroughly studied, especially in perspective of applying physical long-term instability models to the instability-aware design of display circuits.

In this paper, a calculation method for NBIS instability in a-IGZO TFTs is proposed and demonstrated with two kinds of cases with oxygen contents in active layers, i.e., oxygen-poor (O-poor) and oxygen-rich (O-rich) devices. The proposed method effectively enables reproducing the NBIS time (t_{NBIS}) evolution of current–voltage (I–V) characteristics only from the pristine density-of-subgap states (DOS) and NBIS condition even without long-term stress test and is very applicable to general amorphous oxide TFTs along with the process-/material-dependent DOS parameters.

Manuscript received October 11, 2017; revised December 11, 2017; accepted January 13, 2018. Date of publication February 5, 2018; date of current version February 22, 2018. This work was supported in part by the National Research Foundation of Korea funded by the Korean Government (MSIP) under Grant 2016R1A5A1012966 and in part by the Ministry of Education, Science and Technology under Grant 2017R1A2B4006982. The review of this paper was arranged by Editor K. C. Choi. *(Corresponding author: Dae Hwan Kim.)*

The authors are with the School of Electrical Engineering, Kookmin University, Seoul 136-702, South Korea (e-mail: drlife@kookmin.ac.kr).

Color versions of one or more of the figures in this paper are available online at http://ieeexplore.ieee.org.

Digital Object Identifier 10.1109/TED.2018.2797208

II. Calculation Method for the NBIS ΔV_T

The NBIS instability mechanism of a-IGZO TFT can be classified into following three types.

1) The optical illumination-generated holes or positive charged species followed by their trapping into gate insulator/interface as shown in Fig. 1(a), i.e., $(h\nu) \rightarrow e^- + h^+$ with h = Plank's constant and ν = frequency of photon [4], [5].
2) The donor creation by oxygen vacancy ionization as depicted in Fig. 1(b), i.e., $V_O + (h\nu) \rightarrow V_O^{2+} + 2e^-$ or $V_O^{1+} + 1e^-$ [6], [7].
3) The donor creation by the hole-mediated formation of the metastable peroxide defects as described in Fig. 1(c), i.e., $O^{2-} + O^{2-} + (h\nu) \rightarrow O_2^{2-} + 2e^-$ [8].

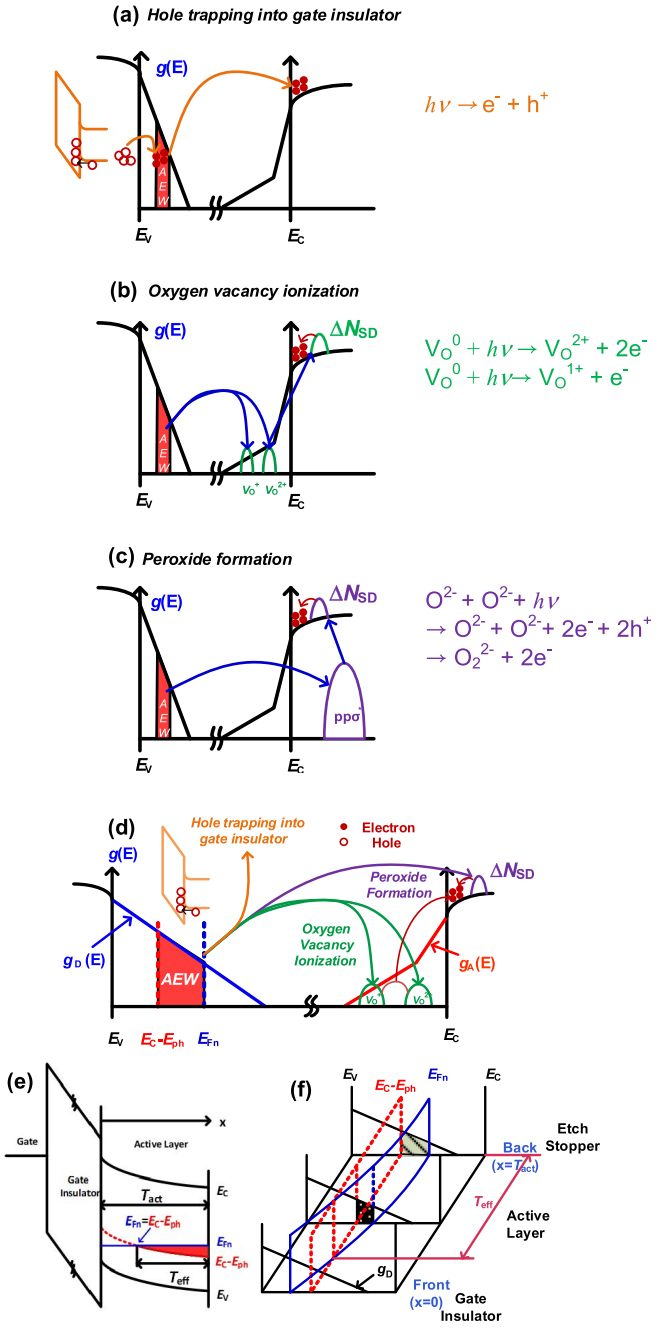

Fig. 1. Schematic illustrations of (a) charge trapping, (b) oxygen vacancy ionization, and (c) peroxide formation models. Schematic of (d) NBIS-induced instability mechanisms correlated with the DOS and AEW, (e) EBD under NBIS, and (f) method for calculating the AEW along a channel depth direction.

The interaction between oxide TFT and ambient [9] was excluded from possible mechanisms due to the presence of robust passivation layer [10].

The valence band tail states (VBTs) of a-IGZO are located in the levels under mid-gap and consist of the (intrinsic) $pp\sigma^*$ antibonding defects [8] and the (extrinsic) oxygen vacancy-related defects [7], [11]. When the device is under a negative gate bias stress, the electron quasi-Fermi energy level E_{Fn} is located in VBTs. Therefore, the NBIS-induced ΔV_T is determined by how many subgap states exist in the energy range between E_{Fn} and E_C–E_{ph}, i.e., activation energy window (AEW) shown in Fig. 1(d), regardless of what the dominant instability mechanism is. Here, E_C, E_V, and E_{ph} are defined to be the conduction band minimum level, the valence band maximum level, and the photon energy.

Fig. 1(e) and (f) shows the energy band diagrams (EBDs) under the NBIS. Here, the density of VBTs is symbolized as $g_D(E)$ [$eV^{-1}cm^{-3}$], which will be shown in Fig. 1(d). Then, AEW can be derived from the following equation:

$$\mathrm{AEW} = \frac{\int_{T_{act}-T_{eff}}^{T_{act}} \int_{E_C-E_{ph}}^{E_{Fn}} g_D(E)\,dE\,dx}{T_{eff}} \tag{1}$$

where x, T_{act}, and T_{eff} are the position coordinate along the direction of TFT channel depth, the thickness of TFT active layer, and the effective thickness of the AEW. Here, T_{eff} means the effective thickness of IGZO film where the degradation occurs under NBIS and it varies with the increase of t_{NBIS} as well as by changing the device structure, stress bias, photoillumination condition, and active material because it manifests itself that the AEW plays as a function of the process/material parameters via a pristine $g_D(E)$, NBIS condition via E_{ph}, and the geometry of TFTs via T_{act}. The E_{Fn} and T_{eff} are then determined by specific conditions of $g_D(E)$, E_{ph}, and T_{act}.

The calculated AEW can be transformed into increasing the concentration of shallow donor (N_{SD}) by ΔN_{SD} and makes it possible to estimate the t_{NBIS} evolution of TFT I–V characteristics as follows.

If the AEW at $t = t_0$ (pristine state), i.e., before applying NBIS, is an AEW(t_0), the ΔV_T during Δt under NBIS is determined by $\Delta N_{SD}(t = t_0 + \Delta t)$. In other word, the AEW(t_0) is identical to the increase of shallow donor concentration in active layer (ΔN_{SD}) between adjacent time spots $t = t_0$ and $t = t_0 + \Delta t$ as follows:

$$\begin{aligned}\mathrm{AEW}(t_0) &= \Delta N_{SD}(t = t_0 + \Delta t) \\ &= N_{SD}(t = t_0 + \Delta t) - N_{SD}(t = t_0).\end{aligned} \tag{2}$$

Therefore, the t_{NBIS} evolution of AEW(t) can be calculated as

$$\begin{aligned}&\mathrm{AEW}(t_i) \\ &= \frac{\int_{T_{act}-T_{eff}(t_i)}^{T_{act}} \int_{E_C-E_{ph}}^{E_{Fn}(t_i)} g_D(E)\,dE\,dx}{T_{eff}(t_i)} \\ &= \Delta N_{SD}(t = t_i + \Delta t) = N_{SD}(t = t_{i+1}) - N_{SD}(t = t_0) \qquad (3) \\ &\mathrm{AEW}(t_{i+1}) - \mathrm{AEW}(t_i) \\ &= N_{SD}(t_{i+2}) - N_{SD}(t_{i+1}) \\ &= \frac{\int_{T_{act}-T_{eff}(t_{i+1})}^{T_{act}} \int_{E_C-E_{ph}}^{E_{Fn}(t_{i+1})} g_D(E)\,dE\,dx}{T_{eff}(t_{i+1})} \\ &\quad - \frac{\int_{T_{act}-T_{eff}(t_i)}^{T_{act}} \int_{E_C-E_{ph}}^{E_{Fn}(t_i)} g_D(E)\,dE\,dx}{T_{eff}(t_i)} \\ &\approx \frac{\int_{T_{act}-T_{eff}(t_i)}^{T_{act}} \int_{E_{Fn}(t_i)}^{E_{Fn}(t_{i+1})} g_D(E)\,dE\,dx}{T_{eff}(t_i)} \qquad (4)\end{aligned}$$

where t_i is a specific time spot under NBIS and t_{i+1} is $t_i + \Delta t$.

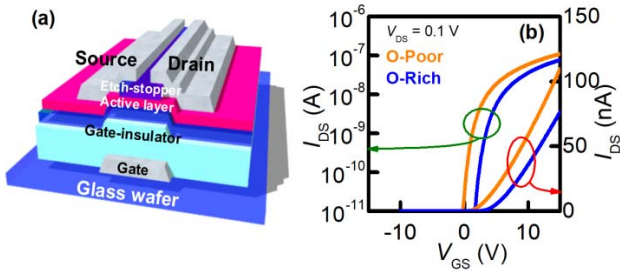

Fig. 2. (a) Schematic illustrations of fabricated a-IGZO TFT. (b) Transfer characteristics with oxygen gas flow rate.

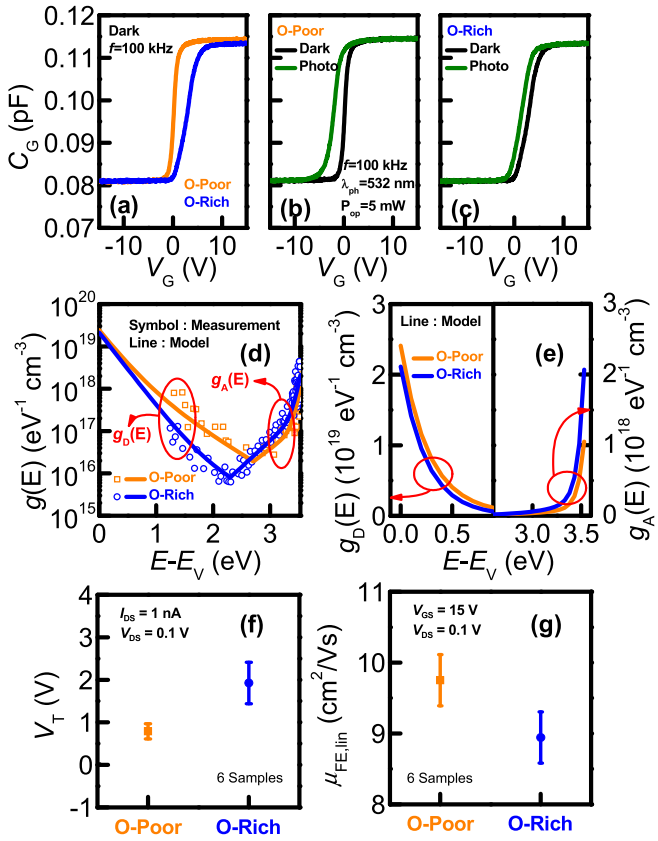

Fig. 3. (a) Measured C–V characteristics at dark ambient. The measured photoresponses of C–V characteristics in (b) O-poor and (c) O-rich TFTs. Extracted DOSs (d) in a logarithm and (e) linear scale. The oxygen-content-dependent (f) V_T and (g) $\mu_{FE,lin}$ extracted at I_{DS} = 1 nA and V_{GS} = 15 V/V_{DS} = 0.1 V from the measurement for six samples of each oxygen gas flow rate condition.

Here, it should be noted that one can calculate all of $E_{Fn}(t_i)$, AEW(t_i), V_T, and I–V characteristics from $g_D(E)$ and $N_{SD}(t = t_i)$ at a specific time spot by using our previously reported I–V model and TCAD simulator [12], [13]. Therefore, we can also calculate either the area of AEW or the I–V characteristic as a function of t_{NBIS} by iterating numerically this procedure with an infinitesimal Δt.

III. Experimental Results and Discussion

The a-IGZO TFT devices have the inverted staggered bottom-gate structure with an etch-stop layer as shown in Fig. 2(a). The sputter-deposited molybdenum (Mo) was used as a metal for gate, source, and drain electrodes. A 400-nm-thick SiO_x layer and a 50-nm-thick SiN_x layer were deposited by plasma-enhanced chemical vapor deposition (PECVD) forming the gate insulator. Then, in order to control the oxygen contents in active layers, a 50-nm-thick IGZO was deposited as TFT active layer by dc sputtering with the gas flow rate of Ar/O_2 = 35/21 sccm (O-poor) and 35/63 sccm (O-rich) at a total pressure of 5 mtorr. Moreover, the sputtering power was controlled to be 2 kW at room temperature. A 50-nm-thick SiO_x etch-stop layer was deposited by PECVD and patterned by wet etching. For the formation of source/drain (S/D) electrodes, Mo is sputtered at room temperature and patterned by dry etching. Finally, the fabricated devices were thermally annealed at 250 °C for 1 h.

The channel width (W) and length (L) of the devices were 100 and 100 μm, respectively. In addition, all I–V and capacitance–voltage (C–V) characteristics were measured at room temperature through the Agilent 4156C semiconducting parameter analyzer and the Agilent 4284A precision LCR meter, respectively. The C–V curve was measured between the gate and the S/D tied each other as a function of gate voltage (V_G). The measured transfer characteristics with different oxygen gas flow rates are depicted as shown in Fig. 2(b).

Fig. 3(a) shows the effect of oxygen content on C–V curve measured at a dark ambient, which is attributed to that either the density of subgap traps or the carrier concentration varies with the change of oxygen contents. First, the V_Os play the role of shallow donor in IGZO. Thus, the O-poor device has higher electron concentration, hence a lower V_T. Therefore, the V_G point where the capacitance begins to sharply rise shifts to more negative direction in O-poor device compared with O-rich device. Second, the V_G sweeps from negative to positive voltage, which is equivalent with the movement of E_{Fn} from E_V up to E_C. If a larger number of subgap states exist below E_C, the E_{Fn} is harder to lift up to E_C and the slope of dC/dV_G becomes smaller. Therefore, the value of dC/dV_G is smaller in O-rich device [higher $g_A(E)$] than that in O-poor device [lower $g_A(E)$] as will be discussed in Fig. 3(d) and (e).

In order to calculate the AEW, we then extracted DOS based on the photoresponse of TFT C–V characteristics. The latter technique is referred as monochromatic photonic C–V spectroscopy [14], and the I–V characteristics were calculated by DeAOTS [12]. Fig. 3(b) and (c) shows the measured photoresponses of C–V characteristics, the conditions of which are as follows: small-signal frequency of 100 kHz, illumination wavelength of 532 nm, and optical power of 5 mW. The DOSs of two devices (O-poor and O-rich) are extracted as indicated in Fig. 3(d) and (e) from the photoresponses of C–V shown in Fig. 3(b) and (c). It is found that the total DOS [$g(E)$] consists of the donor-like DOS [$g_D(E)$] near E_V and the acceptor-like DOS [$g_A(E)$] near E_C. The related details of extraction can also be found in [14].

The material and DOS parameters which were used in our I–V simulation are summarized in Table I. The bandgap (E_g) was taken from spectroscopic ellipsometry. The value of effective DOS (N_C) is calculated by consideration of electron effective mass (~0.35 m_0), and the value of N_V is

TABLE I
MATERIAL AND DOS PARAMETERS MEASURED FROM THE DEVICES

Parameter	Value		Unit
Device	O-Poor	O-Rich	
E_g	3.53		eV
Effective DOS in CBM, N_C	1×10^{19}		cm^{-3}
Effective DOS in VBM, N_V	2.28×10^{20}	1.17×10^{20}	cm^{-3}
N_{SD}	2.6×10^{16}	1.5×10^{16}	cm^{-3}
Acceptor-like DOS	$g_A(E)=N_{TA}\times\exp\left(\frac{E-E_C}{kT_{TA}}\right)+N_{DA}\times\exp\left(\frac{E-E_C}{kT_{DA}}\right)$		
N_{TA}	9.2×10^{17}	1.8×10^{18}	$eV^{-1}cm^{-3}$
kT_{TA}	0.06	0.06	eV
N_{DA}	1.3×10^{17}	2.7×10^{17}	$eV^{-1}cm^{-3}$
kT_{DA}	0.43	0.35	eV
Donor-like DOS	$g_D(E)=N_{TD}\times\exp\left(\frac{E_V-E}{kT_{TD}}\right)+N_{DD}\times\exp\left(\frac{E_V-E}{kT_{DD}}\right)$		
N_{TD}	2.1×10^{19}	2.1×10^{19}	$eV^{-1}cm^{-3}$
kT_{TD}	0.25	0.25	eV
N_{DD}	3.1×10^{18}	1.3×10^{17}	$eV^{-1}cm^{-3}$
kT_{DD}	0.53	0.75	eV

calculated from $N_C \times (N_{TD}/N_{TA})$ [12]. The value of N_{SD} is taken by adjusting its value with numerical iteration until the calculated I–V characteristics agree well with the measured ones. Used I–V model was given in [12] and [13]. All of the DOS parameters are taken from fitting the model equation [line in Fig. 3(d) and Table I] with experimentally extracted DOS [symbol in Fig. 3(d)].

It is found in Fig. 3(d) and (e) that the extracted $g_D(E)$ of O-poor IGZO TFT is higher than that of the O-rich device. The difference of $g_D(E)$ between the O-poor and O-rich devices is prominent, especially in the level around E_V+1 eV. It suggests that a larger amount of neutral oxygen vacancy defects exists in the O-poor TFT in comparison with O-rich TFT [11]. Moreover, it was found that the $g_D(E)$ near E_V is correlated with neutral oxygen vacancy defect through a dependence of photoconductivity characteristics with the oxygen gas flow rate in [15]. On the other hand, the density of acceptor-like traps near E_C, i.e., $g_A(E)$, is higher in O-rich rather than in O-poor TFTs, which is attributed to more severe ion bombardment (higher total flow rate of gas) during the dc sputtering [16]. It is consistent that in comparison with O-rich device, the photoresponse of O-poor device is larger due to the higher $g_D(E)$ as depicted in C–V characteristics of Fig. 3(b) and (c).

From the measurements for six samples shown as the symbols in Fig. 3(f) and (g), it is observed that the O-poor device has the definitely lower V_T and higher $\mu_{FE,lin}$ than the O-rich device, where the V_T and $\mu_{FE,lin}$ (μ_{FE} extracted in a linear region) are extracted at the $I_{DS} = 1$ nA and $V_{GS} = 15$ V/$V_{DS} = 0.1$ V, respectively. Lower V_T and higher $\mu_{FE,lin}$ of the O-poor device are well correlated with larger amount of V_Os and lower $g_A(E)$ than the O-rich device.

Noticeably, the extracted DOS is validated by comparing DOS-based simulated I–V characteristics with the measured pristine I–V characteristics [the black lines and black symbols shown in Fig. 4(a) and (c)].

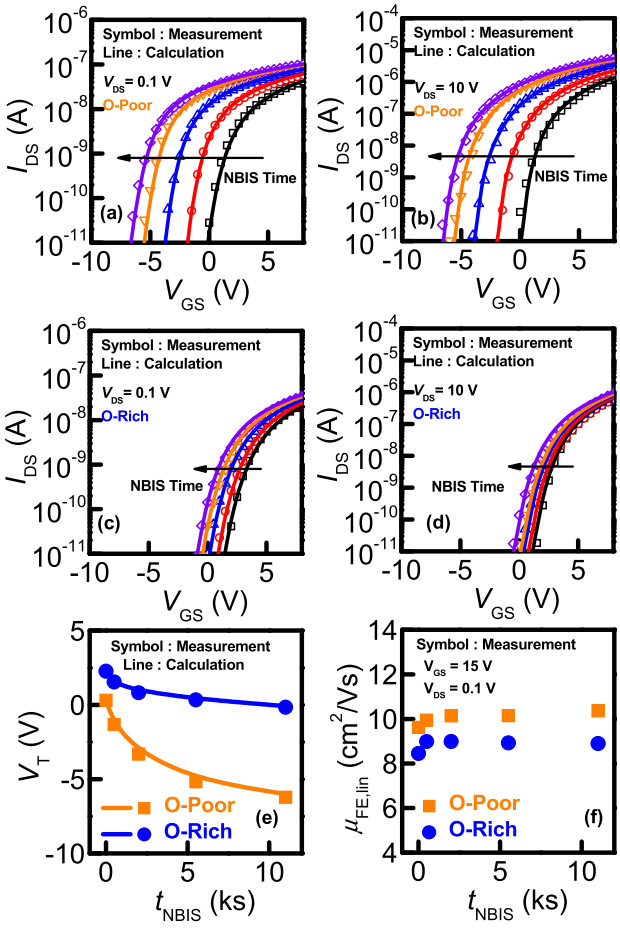

Fig. 4. Measured and calculated t_{NBIS} dependence of I–V characteristics of (a) and (b) O-poor and (c) and (d) O-rich TFTs where (a) and (c) $V_{DS} = 0.1$ V and (b) and (d) $V_{DS} = 10$ V. The t_{NBIS}-dependent (e) V_T and (f) $\mu_{FE,lin}$ from I–V characteristics under $V_{GS} = 15$ V and $V_{DS} = 0.1$ V.

The measured t_{NBIS} evolution of I–V characteristics of a-IGZO TFTs are shown as symbols in Fig. 4(a)–(d), where the conditions of NBIS are $V_{GS} = -20$ V, $V_{DS} = 10$ V, illumination by a commercial LED backlight unit with brightness of 300 cd/m^2. Also, the measured t_{NBIS} evolutions of V_T and $\mu_{FE,lin}$ are shown as the symbols in Fig. 4(e) and (f). While the $\mu_{E,lin}$ remains nearly unchanged during NBIS, the magnitude of NBIS-induced ΔV_T is much smaller in O-rich device than in O-poor device, which is consistent with [17] and [18].

In order to verify our calculation method, the t_{NBIS} evolutions of I–V characteristics were calculated by using the DOS/AEW-based model which is proposed in Section II. The parameters used in calculating the NBIS instability are summarized in Table II, where the E_{FB}, V_{FB}, μ_{Band}, and $E_{ph,eff}$ are the value of difference between E_C and E_{Fn} at a flat band condition, flat band voltage, conduction band electron mobility, and effective photon energy, respectively [12]. As denoted by the lines in Fig. 4(a)–(d), the measured t_{NBIS} evolutions of I–V characteristics are reproduced very well by using the proposed method in O-rich as well as in O-poor device, which suggests that the extracted DOS and the calculation method proposed are reasonable.

TABLE II
PARAMETERS USED IN CALCULATING THE NBIS INSTABILITY

Device	t_{NBIS} [ks]	E_{FB} [eV]	V_{FB} [V]	T_{eff} [nm]	N_{SD} [cm^{-3}]	μ_{Band} [cm^2/Vs]	E_C-$E_{ph,eff}$ [eV]
O-Poor	0	0.308	0.047	26.6	2.6×10^{16}	14.1	2.61
	0.5	0.180	1.161	31.2	4.9×10^{16}		
	2	0.150	2.811	36.2	7.5×10^{16}		
	5.5	0.135	4.022	40.8	10.2×10^{16}		
	11	0.129	5.231	43.8	11.8×10^{16}		
O-Rich	0	0.619	-0.385	17.2	1.5×10^{16}	13.1	2.31
	0.5	0.485	-0.229	19.5	2.3×10^{16}		
	2	0.368	-0.017	21.9	3.3×10^{16}		
	5.5	0.300	0.217	23.5	4.1×10^{16}		
	11	0.262	0.421	24.9	4.7×10^{16}		

The calculated t_{NBIS} dependences of E_{Fn} and E_C–E_{ph} levels are shown as the EBDs in Fig. 5(a) and (b), where the t_{NBIS} is denoted by the legends. It is found that in the case of O-rich devices, the variation of E_C–E_{ph} levels during NBIS is larger than O-poor devices, which can be explained as follows. The $g_D(E)$ is higher in O-poor device rather than in O-rich device. It means that at the same bias condition, the localized charge density is lower in O-rich device than in O-poor device. In turn, the free carrier charge density should be higher in O-rich device. Therefore, in O-rich device, the E_C is modulated larger either by the same change of gate voltage or during the same NBIS time.

Thus, as shown in Fig. 5(a) and (b), the variation of E_C–E_{ph} level is larger, i.e., the band bending is more prominent during NBIS, in O-rich device rather than in O-poor device. Then, the area of AEW is smaller in O-rich device than in O-poor device. Consistently, the calculated t_{NBIS} evolutions of T_{eff} and AEW are shown in Fig. 5(c) and (d). An AEW, which is much larger than that of the O-rich devices, in the O-poor device, clearly explains the reason of the O-poor device being less stable under the NBIS than the O-rich device.

In terms of the validity of AEW calculation, it should be noted that the proposed method is available only on the condition that the number of incident photons is larger than the number of subgap states in AEW. In our case, the number of incident photons from commercial backlight unit was 1.4×10^{15} cm^{-2}s^{-1}. On the other hand, the number of subgap states in AEW was 1.3×10^{11} cm^{-2} (O-poor device) and 7.5×10^{10} cm^{-2} (O-rich device), respectively. Therefore, the used condition is reasonable. This condition works well for general NBIS cases with considering the density of subgap traps in IGZO and the photoillumination environments in commercial displays.

Based on the t_{NBIS} dependence of AEW, it is found that we can calculate the NBIS-induced ΔV_T [lines in Fig. 4(e)] and the stress time evolution of I–V characteristics [lines in Fig. 4(a)–(d)]. It suggests that the proposed calculation method can precisely estimate the I–V characteristics as well as the ΔV_T only from the pristine DOS and NBIS condition, i.e., without long-term stress test.

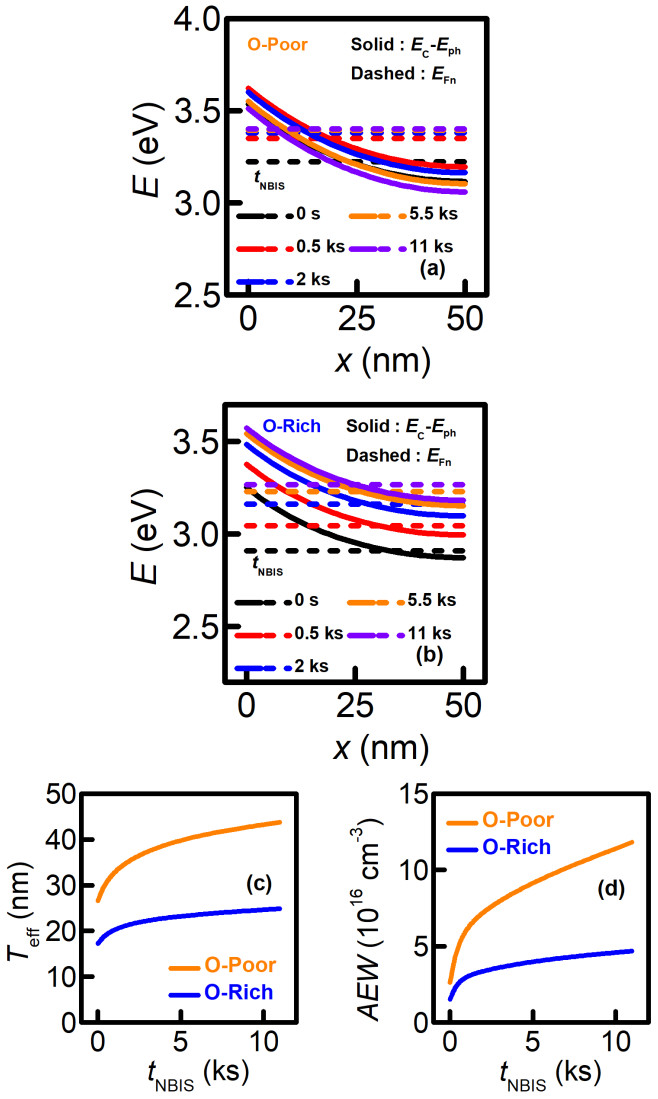

Fig. 5. Calculated t_{NBIS} dependences of E_{Fn} and E_C–E_{ph} levels of (a) O-poor and (b) O-rich TFTs. The t_{NBIS} dependences of (c) T_{eff} and (d) AEW.

It is definitely noteworthy that one wants to calculate the V_T and I–V characteristics during NBIS only from the pristine DOS and illumination condition, i.e., without long-term NBIS test. Furthermore, the NBIS-induced ΔV_T can be described via AEW with the exact function of not only the material/process parameters, e.g., $g_D(E)$, E_g, $g_A(E)$, and N_{SD}, the device geometric parameters, such as the T_{act}, W, L, and gate insulator thickness, but also the stress conditions, such as the stress gate bias and E_{Fn} at bias stress, and the illumination condition, i.e., E_{ph}. The pristine DOS is also determined mainly by the fabrication process and material nature.

For instance, as shown in Fig. 6, the TFT-B which has a relatively smaller area of the AEW shows a smaller NBIS-induced ΔV_T under specific stress conditions than the ΔV_T of the TFT-A which has a relatively larger area of the AEW compared with that of TFT-B. Furthermore, the stress time evolution of all electrical characteristics can also be calculated precisely by using our methodology and parameter set.

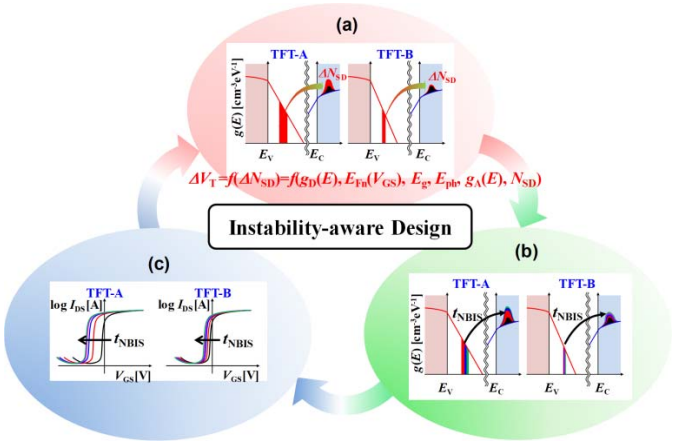

Fig. 6. Concepts of instability-aware design and closed loop.

IV. Conclusion

Our proposed method, which systematically calculate the NBIS ΔV_T in a-IGZO TFTs, was successfully demonstrated through two kinds of specific devices, i.e., O-poor and O-rich devices. Moreover, the effect of oxygen content of a-IGZO on NBIS instability was quantitatively explained very well based on microscopic origins.

Our results suggest that the t_{NBIS} evolution of I–V characteristics can be calculated from the pristine DOS and AEW before applying NBIS. Therefore, the proposed method is potentially useful for calculating/projecting the t_{NBIS} evolution of I–V characteristics without long-term NBIS test, which is the essence of instability-aware design. The closed loop in Fig. 6 also suggests that we can both design highly stable oxide TFTs systematically and optimize all the oxide material, fabrication process, and TFT device structure very efficiently. This is the other essence of instability-aware design.

Acknowledgment

The CAD software was supported in part by SILVACO and in part by the IC Design Education Center.

References

[1] T. Kamiya, K. Nomura, and H. Hosono, "Present status of amorphous In–Ga–Zn–O thin-film transistors," *Sci. Technol. Adv. Mater.*, vol. 11, no. 4, p. 044305, Sep. 2010, doi: 10.1088/1468-6996/11/4/044305.

[2] J. F. Wager, "Flat-panel-display backplanes: LTPS or IGZO for AMLCDs or AMOLED displays?" *Inf. Display*, vol. 30, no. 2, pp. 26–29, 2014.

[3] J. S. Park, W.-J. Maeng, H.-S. Kim, and J.-S. Park, "Review of recent developments in amorphous oxide semiconductor thin-film transistor devices," *Thin Solid Films*, vol. 520, no. 6, pp. 1679–1693, Jan. 2012, doi: 10.1016/j.tsf.2011.07.018.

[4] K. H. Ji *et al.*, "Comparative study on light-induced bias stress instability of IGZO transistors with SiN_x and SiO_2 gate dielectrics," *IEEE Electron Device Lett.*, vol. 31, no. 12, pp. 1404–1406, Dec. 2010, doi: 10.1109/LED.2010.2073439.

[5] J.-Y. Kown *et al.*, "The impact of gate dielectric materials on the light-induced bias instability in Hf–In–Zn–O thin film transistors," *Appl. Phys. Lett.*, vol. 97, no. 18, p. 183503, Nov. 2010, doi: 10.1063/1.3513400.

[6] A. Janotti and C. G. Van de Walle, "Oxygen vacancies in ZnO," *Appl. Phys. Lett.*, vol. 87, no. 12, p. 122102, Sep. 2005, doi: 10.1063/1.2053360.

[7] P. Migliorato, M. D. H. Chowdhury, J. G. Um, M. Seok, and J. Jang, "Light/negative bias stress instabilities in indium gallium zinc oxide thin film transistors explained by creation of a double donor," *Appl. Phys. Lett.*, vol. 101, no. 12, p. 123502, Sep. 2012, doi: 10.1063/1.4752238.

[8] H.-H. Nahm, Y.-S. Kim, and D. H. Kim, "Instability of amorphous oxide semiconductors via carrier-mediated structural transition between disorder and peroxide state," *Phys. Status Solidi B*, vol. 249, no. 6, pp. 1277–1281, Feb. 2012, doi: 10.1002/pssb.201147557.

[9] J. K. Jeong, H. W. Yang, J. H. Jeong, Y.-G. Mo, and H. D. Kim, "Origin of threshold voltage instability in indium-gallium-zinc oxide thin film transistors," *Appl. Phys. Lett.*, vol. 93, no. 12, p. 123508, Sep. 2008, doi: 10.1063/1.2990657.

[10] S. Yang *et al.*, "Improvement in the photon-induced bias stability of Al–Sn–Zn–In–O thin film transistors by adopting AlO_x passivation layer," *Appl. Phys. Lett.*, vol. 96, no. 21, p. 213511, May 2010, doi: 10.1063/1.3432445.

[11] A. Nathan, S. Lee, S. Jeon, I. Song, and U. I. Chung, "Transparent oxide semiconductors for advanced display applications," *Inf. Display*, vol. 29, no. 1, pp. 6–11, 2013.

[12] Y. W. Jeon *et al.*, "Subgap density-of-states-based amorphous oxide thin film transistor simulator (DeAOTS)," *IEEE Trans. Electron Devices*, vol. 57, no. 11, pp. 2988–3000, Nov. 2010, doi: 10.1109/TED.2010.2072926.

[13] M. Bae, K. M. Lee, E.-S. Cho, H.-I. Kwon, D. M. Kim, and D. H. Kim, "Analytical current and capacitance models for amorphous indium-gallium-zinc-oxide thin-film transistors," *IEEE Trans. Electron Devices*, vol. 60, no. 10, pp. 3465–3473, Oct. 2013, doi: 10.1109/TED.2013.2278033.

[14] H. Bae *et al.*, "Single-scan monochromatic photonic capacitance-voltage technique for extraction of subgap DOS over the bandgap in amorphous semiconductor TFTs," *IEEE Electron Device Lett.*, vol. 34, no. 12, pp. 1524–1526, Dec. 2013, doi: 10.1109/LED.2013.2287511.

[15] J. T. Jang *et al.*, "Study on the photoresponse of amorphous In–Ga–Zn–O and zinc oxynitride semiconductor devices by the extraction of sub-gap-state distribution and device simulation," *ACS Appl. Mater. Interfaces*, vol. 28, no. 7, pp. 15570–15577, Jun. 2015, doi: 10.1021/acsami.5b04152.

[16] S. Kim *et al.*, "Impact of oxygen flow rate on the instability under positive bias stresses in dc-sputtered amorphous InGaZnO thin-film transistors," *IEEE Electron Device Lett.*, vol. 33, no. 1, pp. 62–64, Jan. 2012, doi: 10.1109/LED.2011.2173153.

[17] K. H. Ji *et al.*, "Effect of high-pressure oxygen annealing on negative bias illumination stress-induced instability of InGaZnO thin film transistors," *Appl. Phys. Lett.*, vol. 98, no. 10, p. 103509, 2011, doi: 10.1063/1.3564882.

[18] S. Y. Park *et al.*, "Improvement in photo-bias stability of high-mobility indium zinc oxide thin-film transistors by oxygen high-pressure annealing," *IEEE Electron Device Lett.*, vol. 34, no. 7, pp. 894–896, Jul. 2013, doi: 10.1109/LED.2013.2259574.

Jun Tae Jang received the B.S. and M.S. degrees in electrical engineering from Kookmin University, Seoul, South Korea, in 2016, where he is currently pursuing the Ph.D. degree with the Department of Electrical Engineering.

Sung-Jin Choi received the M.S. and Ph.D. degrees in electrical engineering from the Korea Advanced Institute of Science and Technology, Daejeon, South Korea, in 2012.

He is currently an Assistant Professor with the School of Electrical Engineering, Kookmin University, Seoul, South Korea.

Dong Myong Kim (S'86–M'88) is currently a Professor with the School of Electrical Engineering, Kookmin University, Seoul, South Korea. His current research interests include fabrication, characterization, modeling of nanostructure silicon devices, III–V compound semiconductor devices, memories, and CMOS RF circuits.

Dae Hwan Kim (M'08–SM'12) received the B.S., M.S., and Ph.D. degrees in electrical engineering from Seoul National University, Seoul, South Korea, in 1996, 1998, and 2002, respectively.

He is currently a Professor with the School of Electrical Engineering, Kookmin University, Seoul. His current research interests include nano-CMOS, oxide and organic thin-film transistors, biosensors, wearable healthcare devices, and emerging memories.